Axial acoustic field along a solid-liquid fluidized bed under power ultrasound

V. Grosjean[a], C. Julcour[a], O. Louisnard[b], L. Barthe[a,*]

[a] Laboratoire de Génie Chimique, Université de Toulouse, CNRS, INP, UPS, Toulouse, France
[b] Centre RAPSODEE, UMR CNRS 5302, Université de Toulouse, Ecole des Mines d'Albi, 81013 Albi Cedex 09, France

Keywords:
Sonoreactor
Acoustic cavitation
Hydrophone
Spectral analysis
Acoustic shielding
Solid suspension

This work investigates the ultrasound propagation within a liquid-solid fluidized bed. The acoustic mapping of the reactor is achieved by means of a hydrophone. A spectral analysis is carried out on the measured signals to quantify the cavitation activity. The effects of several parameters on the spectral power distribution is appraised – including emitted ultrasound power, liquid superficial velocity and solid hold-up. Results show that increasing US power promotes a higher energy transfer from the driving frequency toward the broad-band noise – which is the signature of transient cavitation – and yields a stronger acoustic shielding. The presence of a flow opposite to the acoustic streaming may affect the sonoreactor behavior by sweeping the cavitation bubbles away from the ultrasonic horn. Finally the presence of millimeter sized particles significantly increases wave attenuation, presumably due to viscous losses on the one hand, and through the contribution of their surface defects to bubble nucleation on the other hand. Moreover, the influence of the solid hold-up appears to depend upon the particle material (glass or polyamide).

1. Introduction

The use of power ultrasound (US) has raised a growing interest in chemistry and chemical engineering since the 90's and sonochemistry now covers a large range of applications [1,2]. However, the involved phenomena are of great complexity and make the efficient design of sonoreactors into a hard task. For instance several authors reported a levelling off or even a decrease of US efficiency when increasing the acoustic power [3–5]. This effect, known as "acoustic shielding", is explained by the reduction of active cavitation zones inside the reactor. When the acoustic power is increased, the bubble cloud densifies, which increases the attenuation of the acoustic wave, thus restricting the active zones at the very vicinity of the ultrasonic horn. Knowledge about cavitation zone distribution is paramount to understand the performance of sonoreactors, provides rational designs and extrapolate sono-processes at the industrial scale.

Characterization of sonochemical reactors can be achieved through different techniques, and an exhaustive list can be found in several reviews and books [6–8]. The most common and classic technique is calorimetry, due to its simplicity in use [9,10]. This method quantifies the acoustic power dissipated in the liquid by measuring the time-evolution of temperature in the medium. It is a global method and does not give any information about spatial distribution or level of acoustic cavitation. Dosimetry techniques – using for instance Fricke solution, potassium iodide, nitrophenol or terephthalate – quantify the chemical activity inside the sonoreactor, based on the oxidative activity of $^{\cdot}OH$ radicals formed during the collapses of cavitation bubbles [6–8,11–13]. Again they do not in general provide information about their location.

Some techniques are more focused on the spatial mapping of the sonoreactors. Aluminum foil erosion gives a direct visualization of the local intensity of cavitation [14,15], but it is difficult to define a quantitative criterion from it. Sonoluminescence, or light emission by cavitation bubbles, is a well-known phenomenon that can be utilized for characterization purpose. Yasui et al. [16] describe the state of knowledge about the underlying mechanisms. With an adequate setup it is possible to observe the zones of active cavitation and to quantify their intensity via photo-multipliers [17]. Another linked technique is based on sonochemiluminescence, where acoustic cavitation bubbles produce light by the reaction between the radicals produced during their collapse and luminol added beforehand to the solution [18,19]. A third optical method is laser tomography [12]. By illuminating the reactor with a laser sheet, bubble clouds can be visualized. This technique is easier to set-up than the two previous ones, but it doesn't make any difference between the active bubbles and those which are not. Finally acoustic measurements by a hydrophone can efficiently probe sonoreactors [20]. It usually uses piezo-electric materials (ceramics or

* Corresponding author.
E-mail address: laurie.barthe@ensiacet.fr (L. Barthe).

https://doi.org/10.1016/j.ultsonch.2019.04.028

polymers), converting their deformation by the acoustic pressure into a measurable electric signal. This will be the technique used in this work, as it provides both quantitative and local information without the need of modifying the medium of interest or the reactor, and it is thus is a good candidate as standard characterization technique for industrial set-ups.

The main pitfall of this technique is to properly interpret the measured signals of acoustic pressure. Indeed the acoustic spectrum under ultrasonic cavitation displays a very rich and complex pattern. Many authors agree on the fact that the spectrum measured in a sonoreactor working at a driving frequency f_0 will show lines corresponding to the fundamental frequency (f_0), but also its harmonics (kf_0), sub-harmonics (f_0/n) and ultra-harmonics (kf_0/n), as well as a broad-band noise between those frequency lines [20–24]. Previous works give different explanations about the genesis of those spectrum characteristics, but all agree on two points. First, if the source is strictly monochromatic, the spectrum will not show other characteristics than fundamental frequency unless there are bubbles in the system. Second, the spectrum lines apart from the fundamental frequency are the signature of stable (or long lifetime) cavitation bubbles. The origin of the broad-band spectrum remains an open issue. Most of the authors consider that it is directly produced by the fast collapsing or transient cavitation bubbles. Yasui et al. [25] show by numerical simulations that this broad-band spectrum is due to the fluctuation of the number of bubbles rather than to their chaotic pulsation. Yet in their conclusion, the authors state that this broad-band noise, although not directly produced by shock-waves, is strongly linked with the presence of transient cavitation, as these bubbles can disintegrate into daughter bubbles during their collapse causing the temporal fluctuation of the number of bubbles. Hence many authors define a transient cavitation index based on the quantification of this broad-band noise. One measurement method of this noise considers only the high frequency zone of the spectrum where no more harmonics appear. For example, Hodnett et al. [26,27] apply a band pass filter between $1,5\ MHz$ *and* $8\ MHz$to the signal and then define their cavitation index as the root mean square value of the resulting signal. Similarly, Uchida et al. [28,29] define the cavitation index as the integral of the spectrum over a band located in the high frequency region (here between $1\ MHz$ and $5\ MHz$). An alternative method is to integrate the spectrum on a wider band, after eliminating the lines corresponding to the (sub/ultra) harmonics and/or the fundamental [30]. This last method is more complex to apply as it needs to detect and eliminate specific parts of the spectrum, but it is more rigorous.

As said before, cavitation zone locations are very dependent on how the power ultrasound propagates inside the reactor. The main complexity comes from the sound attenuation due to the very presence of the cavitation bubbles (acoustic shielding). But the medium in a sonoreactor can include more than two phases (solution + bubbles), as many applications use a solid phase (lixiviation, catalytic reactions …). This added solid phase can have an impact on power ultrasound propagation and thus on the location and size of active cavitation zones. The effect of solid suspension on ultrasound propagation is well known in the case of diagnostic ultrasound. There are well-established models [31,32] able to measure the features of solid suspensions (particle size distribution and hold-up) through the measurement of sound propagation. But this area of acoustic, known as acoustic spectroscopy, is limited to low intensity ultrasound. The behavior of power ultrasound in a solid suspension and the respective contributions of bubbles and solid to its attenuation remain mostly unknown.

To answer these issues, this work aims at investigating the propagation of ultrasound in a solid – liquid fluidized bed, made of millimeter-sized particles. This is achieved through an acoustic mapping of the sonoreactor with a hydrophone and an adequate processing of the measured signals. Several operating parameters are explored such as solid concentration, liquid flow rate, emitted power and nature of the solid particles.

Table 1
Solid particle characteristics.

Material	Glass	Polyamide
Diameter (mm)	2	2
Density ($kg.\ m^{-3}$)	2560	1180
Specific heat ($J.\ kg^{-1}.\ K^{-1}$)	753	1600
Thermal conductivity ($Wm^{-1}K^{-1}$)	1.05	0.25
Thermal expansion coefficient (K^{-1})	4.010^{-6}	8510^{-6}

2. Experimental setup

In order to investigate the behavior of power ultrasound in the presence of a solid suspension, an acoustic mapping of a fluidized bed is achieved. A fluidized bed consists in an upward fluid flow (here water) that keeps solid particles into suspension by applying a drag force able to counteract the apparent particle weight. It results into a solid suspension whose concentration is rather uniform in the case of a liquid-solid system, without the need of a mechanical stirrer which could modify the ultrasound propagation. Solid hold-up can be then varied in a wide range by modifying the liquid superficial velocity (i.e. the ratio of the volumetric flow rate Q_L to the cross-sectional area of the reactor S_{bed}). In the present work, two types of particles are used, whose characteristics are given in Table 1.

The reactor is made of PMMA and consists of a $30\ cm$ high and $5\ cm$ diameter wide column, comprising a liquid distributor (made of a $5\ cm$ high fixed bed of $4\ mm$ diameter glass particles) at its bottom to homogenize the incoming flow and an enlargement at the top to reduce the fluid velocity. The upward liquid stream is provided by a centrifugal pump and its flowrate (Q_L up to $750\ L.\ h^{-1}$) is controlled by rotameters, the fluid circulating in a closed circuit. The temperature of the feeding tank is kept at $20\,^{\circ}C \pm 0.5\,^{\circ}C$. A differential manometer enables the measurement of the pressure drop between the base and the top of the fluidized bed with a precision of $10\ Pa$. Power ultrasound is emitted from an ultrasonic horn placed at the top of the column and powered by a generator. The horn/generator couple is provided by Sinaptec to get a driving frequency of $20\ kHz$. The built-in servo control prevents from working below cavitation, and frequency is tuned in a narrow range to maximize the power input in the liquid, resulting in an average value of $19.7 \pm 0.01\ kHz$. The yield of this equipment, measured by calorimetry, is around 80%. The hydrophone is introduced on the side of the column via inserts placed every centimeter to allow spatial mapping along the axis. It is not moved when varying the acoustic power or the liquid flow rate (without particles). The emitting surface of the ultrasonic horn lies $2.5\ cm$ above the first measurement point. A scheme of the experimental setup is illustrated in Fig. 1.

The acoustic signal is measured by a hydrophone designed by the University of Santiago in Chile. The design of this hydrophone is detailed in the paper of Gaete-Garretón et al. [33]. In brief, it consists of a piezoelectric sensor encapsulated at the tip of a $2\ mm$ diameter rod. The hydrophone also includes a built-in electronic providing it with a stable sensitivity over 10–150 kHz range. It should be noticed that the sensitivity provided by the authors [33] was measured without the built-in amplifier, hence $20\ dB$ must be added to the values given in Fig. 2 to obtain the actual sensitivity. The signals measured by the hydrophone are digitized by a numerical oscilloscope (PicoScope model from Pico Technology). They are then processed by a Matlab script in order to get useful information as described in the following part.

3. Acoustic signal processing

3.1. Signal processing steps

The hydrophone output-voltage U, is sampled at 18 MHz by the numerical oscilloscope in order to obtain 32 successive sequences of

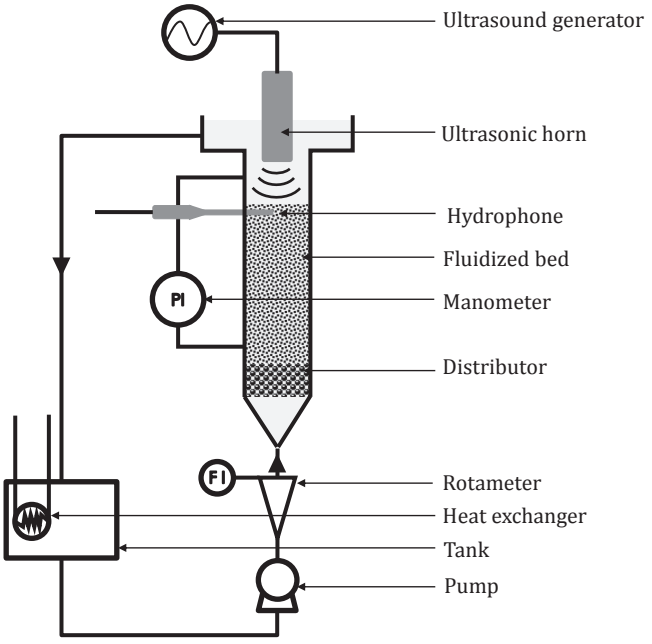

Fig. 1. Experimental setup.

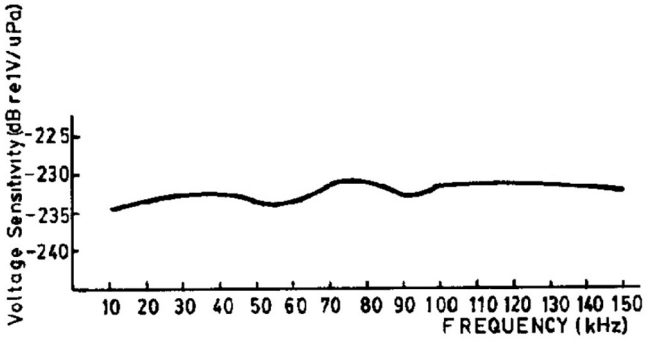

Fig. 2. Hydrophone sensitivity [33].

$T = 50\ ms$ duration. These parameters have been found adequate from a sensitivity study (see below). Each sequence is then windowed and zero-padded before computing the fast Fourier transform. Windowing is used to reduce the amplitude of the side lobes around the peaks of the spectra, which could affect the quantification of the broad-band noise. A Hanning window is applied, which makes a good compromise between the reduction of the side lobes and the increase in width of the main lobe. On the other hand, zero padding is used to enhance the spectral definition. These two steps are shown in Fig. 3.

The Fast Fourier Transform of U is calculated by the dedicated Matlab function and is corrected by subtracting the signal measured in silent condition having undergone the same processing. Only the positive frequency domain of the FFT is considered ($FFT_U(f)$) Using the sensitivity values ($S(f)$) provided by Gaete-Garretón et al. [33] (cf. Fig. 2), the signal spectrum is then converted into pressure unit giving $FFT_p(f)$, the fast Fourier transform of the acoustic pressure in Pa:

$$FFT_p(f) = \frac{FFT_U(f)}{S(f)} \tag{1}$$

Note that the spectra are cut above 150 kHz because the sensitivity of the hydrophone is known only up to that frequency. The FFT is a complex number and only its module ($|\ |$ operator) is of interest in this work. Its argument (the phase of each sinusoidal component) could not be exploited because ultrasound emission and hydrophone acquisition were not synchronized. Then the Power Spectral Density of the acoustic pressure ($PSD_p(f)$ in Pa^2Hz^{-1}) is given by the following expression [34]:

$$PSD_p(f) = 2\frac{|FFT_p(f)|^2}{N_{sig}\ F_S\ W^2} \quad \text{with} \quad \langle W^2 \rangle = \frac{1}{T}\int_0^T W(t)^2 dt \tag{2}$$

In this expression, N_{sig} is the number of signal samples before zero padding, F_S is the sampling frequency, W is the window function, here of Hanning type, and $\langle W^2 \rangle$ the period-average of its squared value (0.375 for Hanning window). The multiplicative "2" factor arises from the symmetry property of the FFT (the considered spectra being restricted to the positive frequency range).

Finally the PSD is averaged over the 32 acquisitions according to:

$$\langle PSD_p \rangle(f) = \frac{1}{32}\sum_{i=1}^{32} PSD_{p_i}(f) \tag{3}$$

Peaks corresponding to the (sub/ultra) harmonics and the fundamental are extracted with the Matlab built-in peak detection algorithm. The extracted peaks are those corresponding to the driving frequency f_0 and the (sub/ultra) harmonics multiple of f_0 and $\frac{1}{2}f_0$, up to $7f_0$ which is the last harmonics below $f_{max} = 150\ kHz$. The width of each peak is taken as twice the full width at half maximum (Δf) and their (P_{peak}) is calculated by integrating the PSD spectrum over the respective peak-width:

$$P_{peak} = \int_{f_{peak}-\Delta f_{peak}}^{f_{peak}+\Delta f_{peak}} \langle PSD_p \rangle(f) df \tag{4}$$

The total power (P_{tot}) is obtained from integration of the full spectrum up to 150 kHz, and the power relative to the broad-band noise (P_{noise}) is deduced by subtracting that of all the peaks from the total power:

$$P_{tot} = \int_0^{f_{max}} \langle PSD_p \rangle(f) df \tag{5}$$

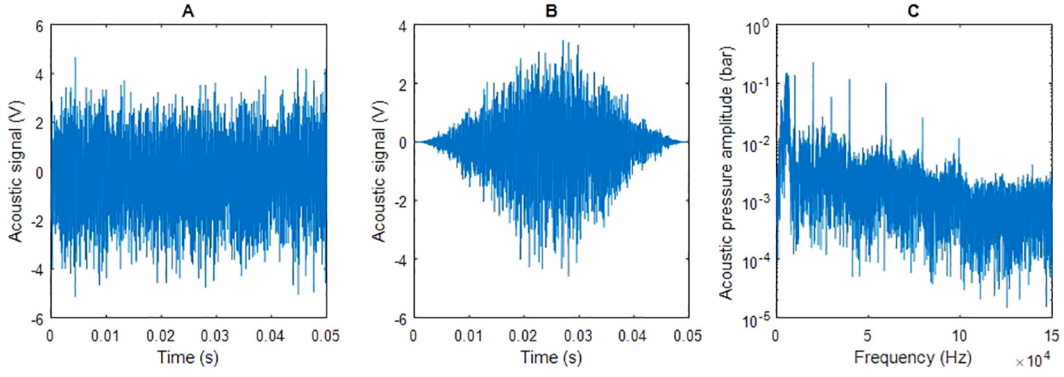

Fig. 3. Signal processing – (A) Oscilloscope signal – (B) Windowed signal – (C) Amplitude spectrum.

$$P_{noise} = P_{tot} - \sum P_{peak} \quad (6)$$

The respective contributions of all components (fundamental, harmonics and broad-band noise) is obtained by dividing each power value by the total power of the spectrum.

The RMS pressure for each component is finally given as the square root of the corresponding power value. Following Parseval's identity, the total power obtained from the PSD integration over the whole frequency range should coincide with that calculated from the temporal signal. We found that the former actually accounts for about 70% of the latter, due to the spectrum cut above 150 kHz.

The amplitude spectrum (AS_p, in Pa), giving the pressure amplitude of each frequency component of the signal, is also calculated as follows:

$$AS_p(f) = 2\frac{|FFT_p(f)|}{N_{sig}\,\langle W\rangle} \text{ with } \langle W\rangle = \frac{1}{T}\int_0^T W(t)dt \quad (7)$$

The average value of the window $\langle W\rangle$ equals 0.5 in the case of a Hanning window. It should be emphasized that the mean amplitude of a given peak calculated over the 32 signals is obtained from averaging the separate AS_p values corresponding to a peak maximum around the expected frequency (i.e. after locating the right peak in each spectrum). Indeed since the driving frequency of the US emitter (continuously adjusted by the servo-control system) can slightly shift from one acquisition to another, simply averaging the 32 amplitude spectra would artificially widen the peaks and hence lower their amplitude.

3.2. Sensitivity analysis on the sampling parameters

A sensitivity analysis has been first carried out regarding the effect of the signal sampling parameters on the results.

First, the sampling frequency of the oscilloscope (18 MHz) is sufficiently high to fulfill Shannon's condition, as the hydrophone has a cutting frequency well below 9 MHz, which excludes any significant line spectrum beyond the latter frequency value.

Fig. 4A shows the effect of the signal duration on the FFT peak magnitude at the driving frequency: the lower the signal duration the wider the peak and the lower its maximum. For a signal duration of 2 ms or less, the amplitude of the peaks is so small that they can't be detected; as a result, the signal appears as exclusively composed of noise (see Fig. 4B). Increasing the signal duration first leads to a minimum in the noise contribution, as the detected peaks are so wide that they cover a significant part of the broad-band noise leading to its underestimation. Beyond 25 ms, the noise contribution finally reaches a plateau.

Averaging the power and amplitude results over several successive acquisitions helps to reduce the randomness of the acoustic signal under cavitation conditions, as illustrated in Fig. 5. The RMS pressure of the total spectrum begins to stabilize with about 10 spectra average and a plateau is almost reached after 32 acquisitions (standard deviation equals 0.6% of the mean between 10 and 32 spectra). Since it represents the maximum memory capacity of the numerical oscilloscope at the set sampling rate and duration, this number of spectra has been used for the further measurements.

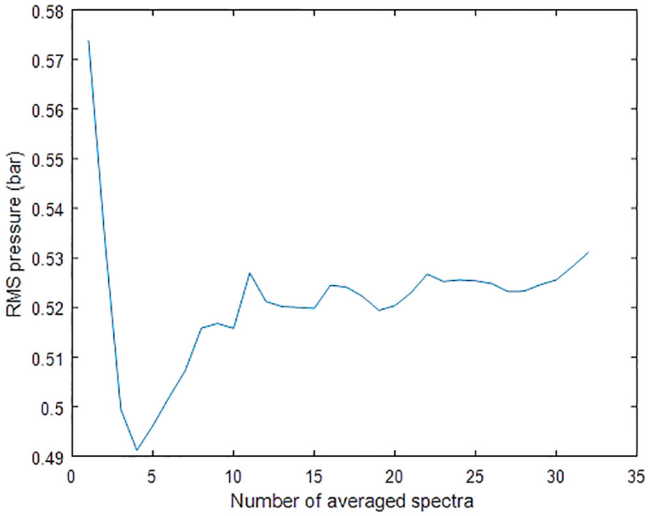

Fig. 5. Effect of the number of averaged spectra on RMS pressure of the total spectrum.

3.3. Repeatability of the measurements

The obtained spectra are typically as illustrated in Fig. 3C. They exhibit a vertical line around 20 kHz corresponding to the driving (fundamental) frequency and vertical lines around multiples of 10 kHz corresponding to various (sub/ultra) harmonics. The broad-band noise lies between those lines. The amplitude/RMS pressure profiles obtained from the processing of the signals measured along the reactor axis are composed of 24 points, spaced of 1 cm and beginning 2.5cm below the surface of the ultrasonic horn.

Repeated tests have been done without solid and without flow for an emitted power of 150 W. Corresponding spatial evolution curves of the RMS pressure, depicted in Fig. 6, are found almost superimposed, no matter which part of the spectrum is considered. Some points located in

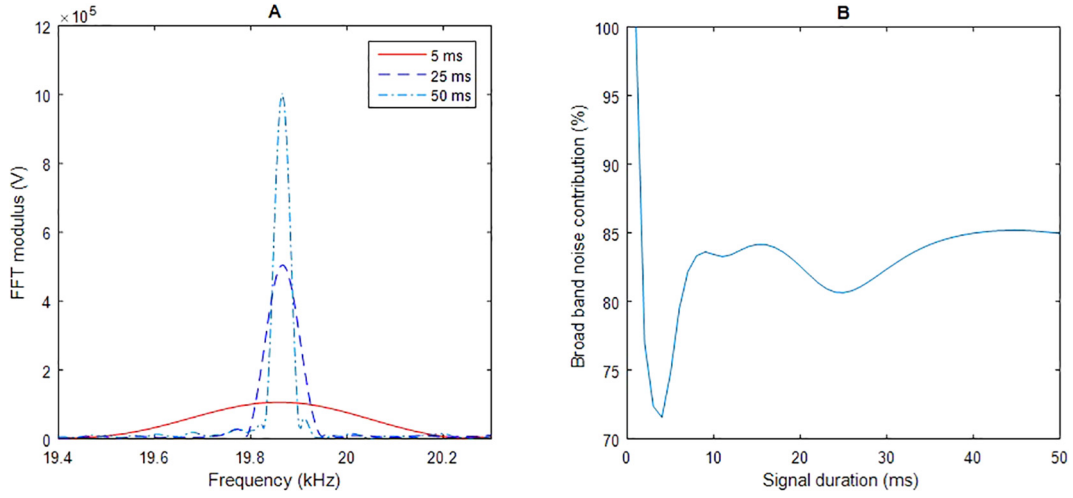

Fig. 4. Effect of the signal duration – (A) on the fundamental peak magnitude – (B) on the broadband noise contribution to the signal power.

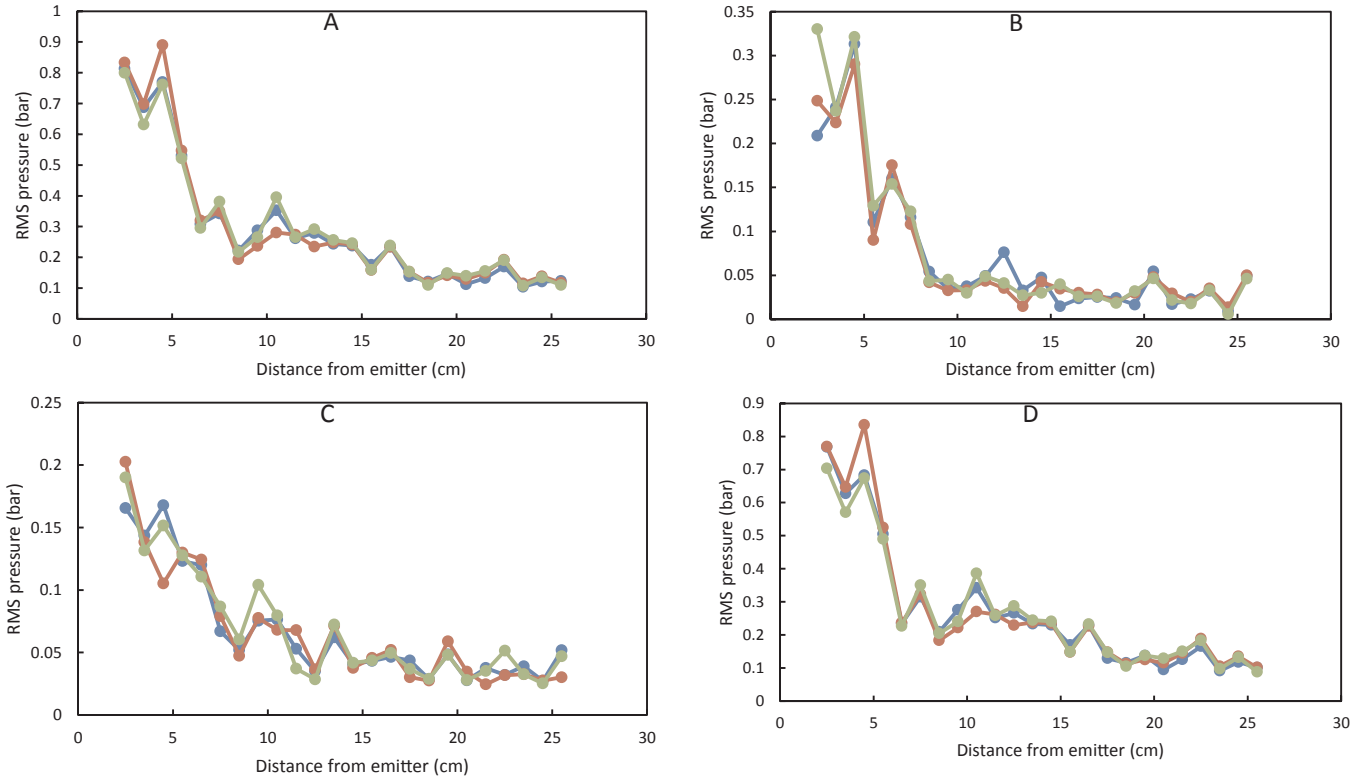

Fig. 6. Repeatability of the RMS pressure vs. axial distance from the emitter curves (emitted US power = 150 W, no solid and no liquid flow, 3 repetitions): (A) Total spectrum, (B) Fundamental, (C) (sub/ultra) Harmonics and (D) Broad-band noise.

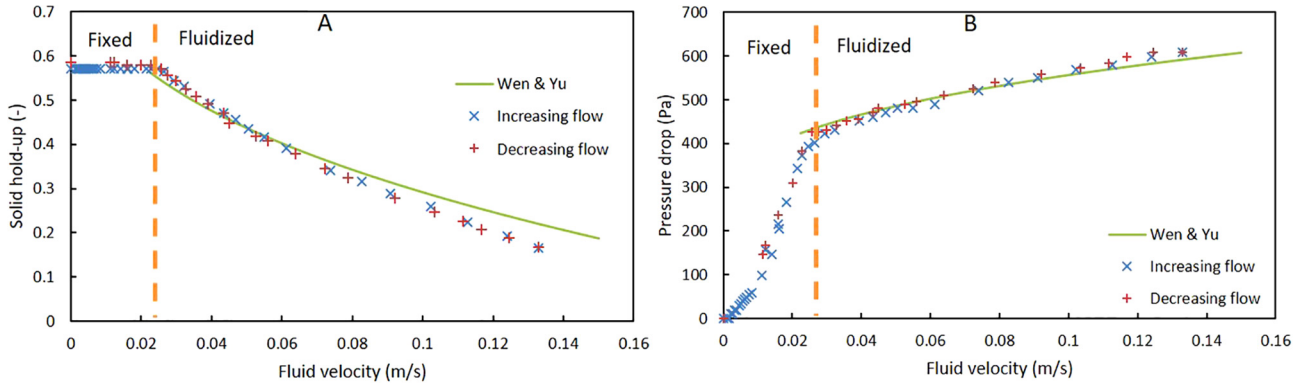

Fig. 7. Fluidization of 2 mm glass beads under silent conditions with increasing and decreasing flow – (A) Solid hold-up – (B) Pressure drop.

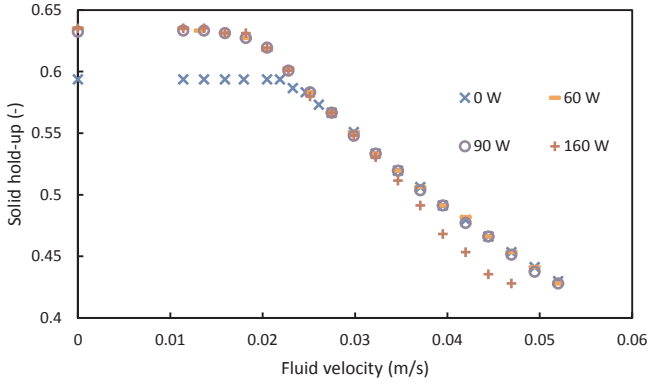

Fig. 8. Fluidization of 2 mm glass beads under power ultrasound with decreasing flow only – Solid hold-up.

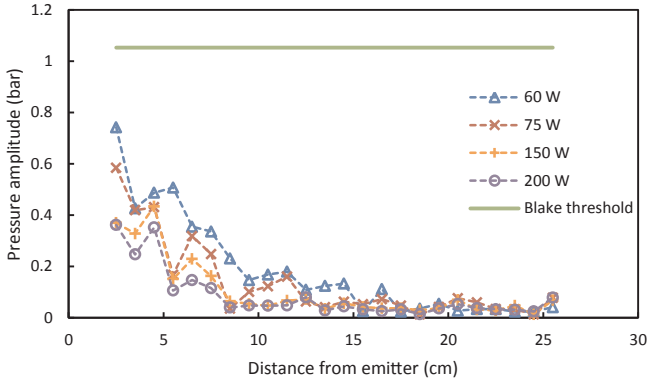

Fig. 9. Effect of emitted US power on the axial evolution of the pressure amplitude at the fundamental frequency (case of non-flowing liquid) and comparison with the value of the Blake threshold calculated for 5 µm diameter bubbles.

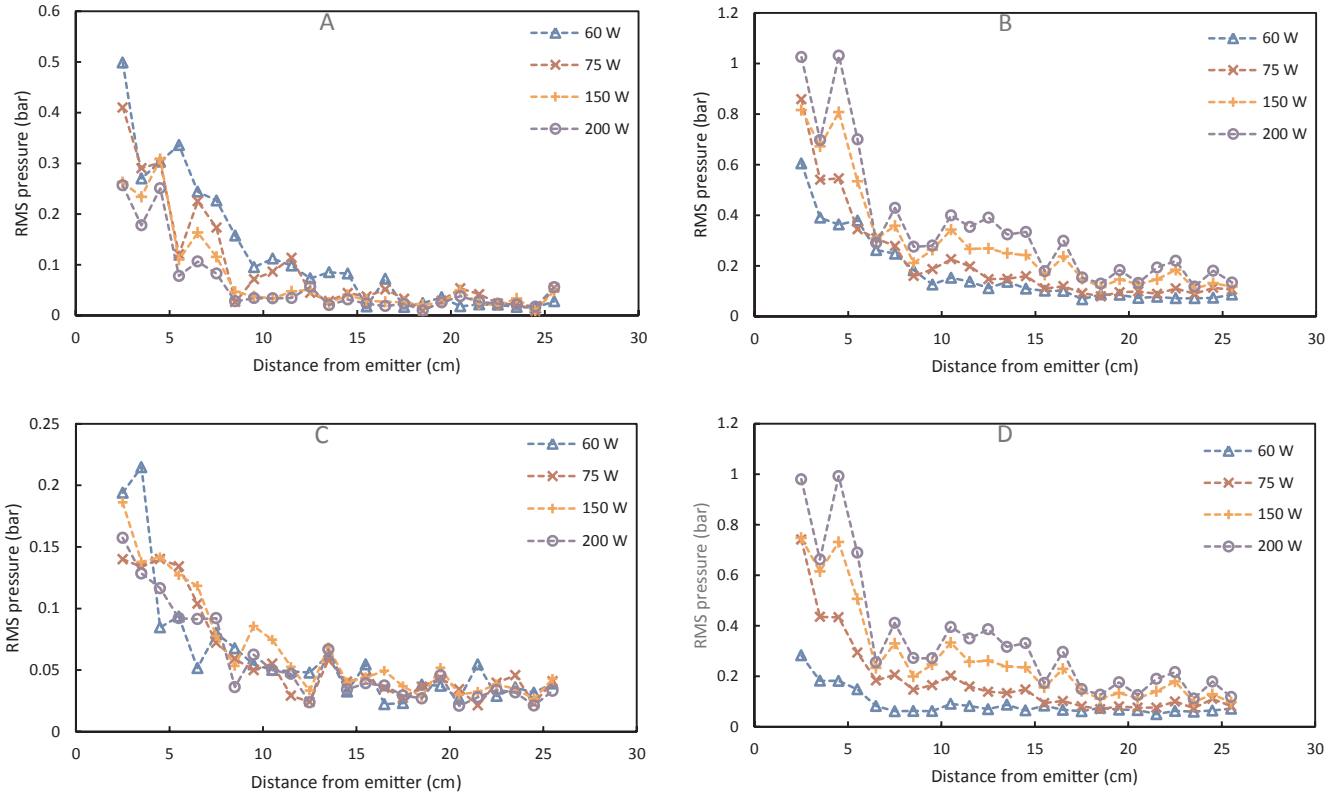

Fig. 10. Effect of emitted US power on the axial evolution of the RMS pressure calculated over different spectrum parts – case of non-flowing liquid – (A) Fundamental frequency– (B) Total spectrum – (C) (sub/ultra) harmonics – (D) Broad-band noise.

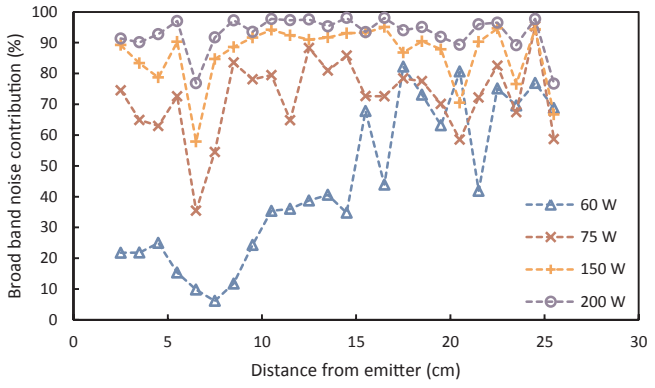

Fig. 11. Effect of emitted US power on the axial evolution of the broad-band noise contribution – case of non-flowing liquid.

the first 5 *cm* exhibit however a stronger variation. This zone coincides with the observed bubble cloud, which could explain the increased deviation of the measurements. Overall, the measurements show 20% deviation, which is small enough to derive reliable trends.

A strong spatial attenuation of all the signals (fundamental, harmonics, and broad-band noise) is observed over the first 10 *cm*, leading to a total RMS pressure reduced by about a factor 5. In this condition of high ultrasonic power, most of the signal consists into broad-band noise.

4. Results

4.1. Behavior of the fluidized bed under ultrasound

The behavior of fluidization under ultrasound is first investigated. The characterization of the fluidized bed is based on the measurement of the solid hold-up and the pressure drop through the bed over a range of liquid velocities. The pressure drop is measured by a differential manometer and the solid hold-up φ (Eq. (8)) is deduced from the measured bed height $h_{bed}(m)$ (the free surface of the expanded bed being located visually):

$$\varphi = \frac{m_p}{\rho_p S_{bed} h_{bed}} \tag{8}$$

with m_p the mass of the solid particles (kg), their density $\rho_p(kg.\ m^{-3})$ and S_{bed} the cross-sectional area of the column (m^2).

The results obtained for the fluidization of 2 *mm* glass beads in silent conditions are gathered in Fig. 7. As a hysteresis behavior could be expected [35,36], measurements have been performed with both an increasing and a decreasing fluid velocity. All the curves exhibit two distinct zones separated by a slope break; they correspond to the two states of the bed: fixed and fluidized. Under silent conditions, the expansion and contraction curves are almost superimposed: the solid hold-up of the fixed bed is only very slightly higher with a gradually decreased flowrate, due to some rearrangement of the particles. The experimental data are also consistent with the Ergun equation for pressure drop in the fixed bed zone [37], and that of Wen and Yu for solid hold-up in the fluidized bed zone [38]. The low increase of pressure drop in the latter region, observed in Fig. 7B, is actually due to the fact that the lowest insert is not at the very base of the column. Thus the mass of solid present between the two pressure measurement points increases with the bed expansion, so does the measured pressure drop. It has been accounted for in the line curve shown in Fig. 7B (using Wen and Yu's expression for solid hold-up).

Power ultrasound emission has little effect on fluidization behavior, as seen in Fig. 8, corresponding to the bed contraction. It further improves the packing of the fixed bed (by about 10%) because of the vibrations, but excepting at the highest US power the bed expansion under fluidization remains almost unchanged. Actually, at 160 W, the

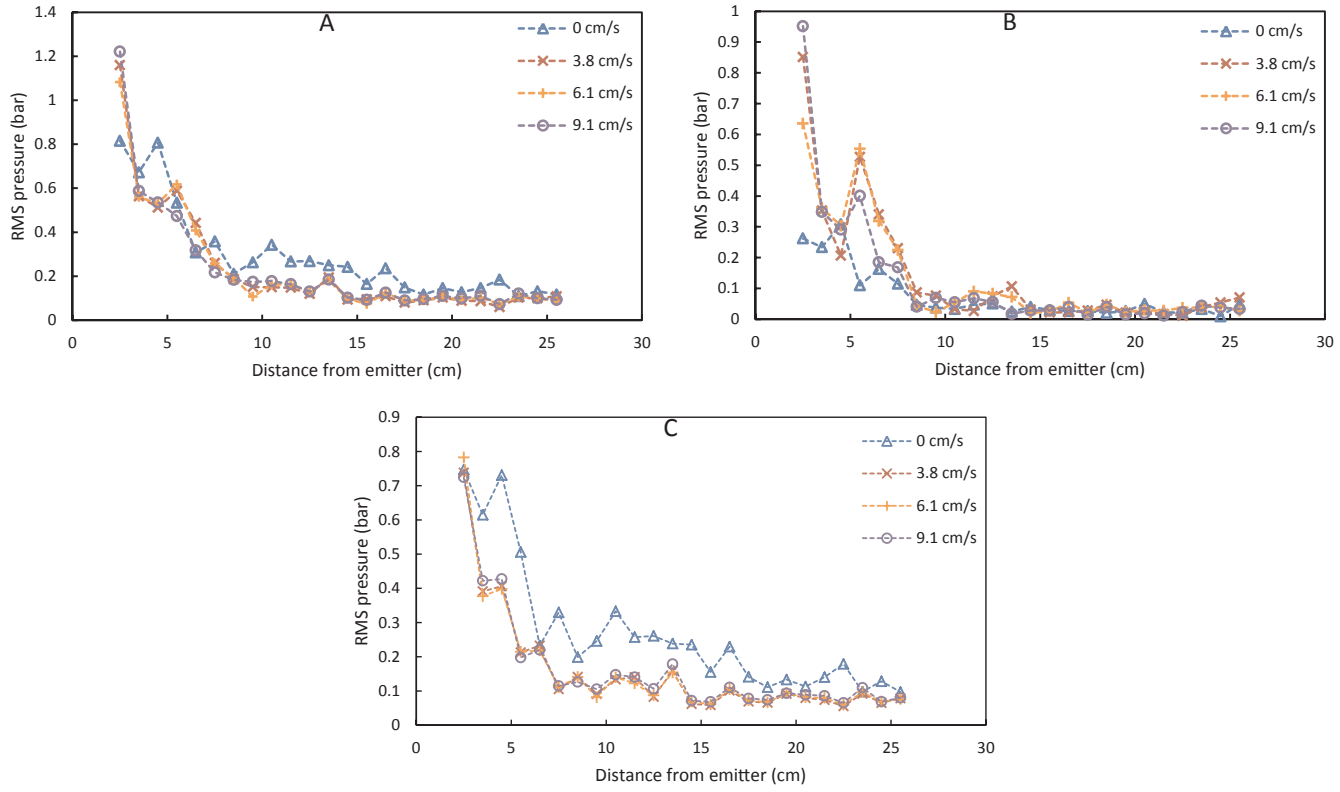

Fig. 12. Effect of liquid velocity on the axial evolution of the RMS pressure calculated over different spectrum parts – case without solid, emitted US power = 150 W – (A) Total spectrum – (B) Fundamental frequency – (C) Broad-band noise.

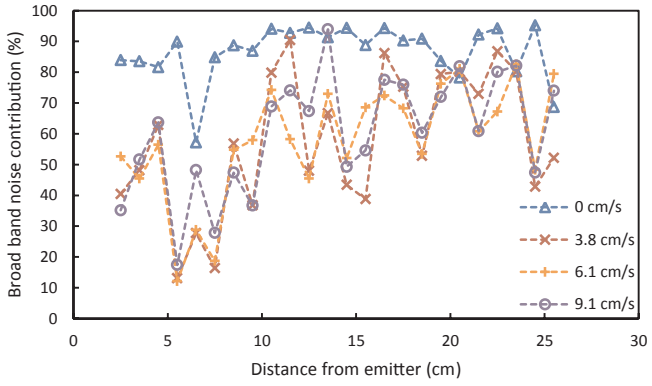

Fig. 13. Effect of liquid velocity on the axial evolution of the broad-band noise contribution – case without solid, emitted US power = 150 W.

Table 2
Attenuation coefficients of 2 mm diameter particles in a 50% vol./vol. aqueous suspension.

Material	Glass	Polyamide
$\alpha_{th}(Np.\ m^{-1})$ [47]	2.7110^{-4}	3.1610^{-6}
$\alpha_{visc}(Np.\ m^{-1})$ [46]	48.810^{-3}	2.110^{-3}

intense acoustic streaming deforms the bed surface, thus making difficult and inaccurate the measurement of its position, and probably leading to an overestimation of its height.

Our primary intention was to measure the pressure drop also under ultrasound, but we observed that the presence of gas bubbles stuck in the liquid line (due to cavitation) jeopardized the accuracy of the differential pressure measurement.

4.2. Parameter study on ultrasound propagation

Different parameters related to the ultrasound emission, the liquid flow conditions and the particle suspension were investigated, and their effects on the spectral power distribution and the signal attenuation are discussed below. For these measurements, the free surface of the expanded bed was set 1.5 *cm* below the US emitter (by adjusting the amount of beads for a given solid hold-up).

4.3. Effect of the acoustic power

Measurements were first performed for the column filled with liquid only and without flow. The signal amplitude at the fundamental frequency vs. depth profile is shown on Fig. 9 for different values of the emitted US power (accounting for the equipment yield measured by calorimetry). The observed tendency could first appear as counter-intuitive, as the profiles at low US power emissions are significantly higher than those at high power. With similar measurements, Son et al. [39] observed that the fundamental amplitude profile is not affected by the emission power. However they worked at lower power (13–40 *W*) and seemed to be in a regime with very low broad-band noise. Considering the Blake threshold as the limit amplitude necessary to explosive growth of bubbles at low US frequency (and assuming for the calculation a uniform radius of 5 μm [40–42]), the most active cavitation zone lays above the first measurement point, so confined in the immediate vicinity of the emitter. However, since the Blake threshold is a model describing the behavior of an isolated bubble, using it to locate cavitation zones might be inaccurate. Indeed some authors like Nguyen et al. [30] measure a cavitation threshold around 20 *kPa* for a frequency of 20 *kHz*.

To explain the effect of the acoustic power an exploration of the rest of the spectral information is needed. If obviously the same decreasing trend can be observed for the fundamental power (Fig. 10A showing equivalent RMS pressure), the RMS pressure associated with the total

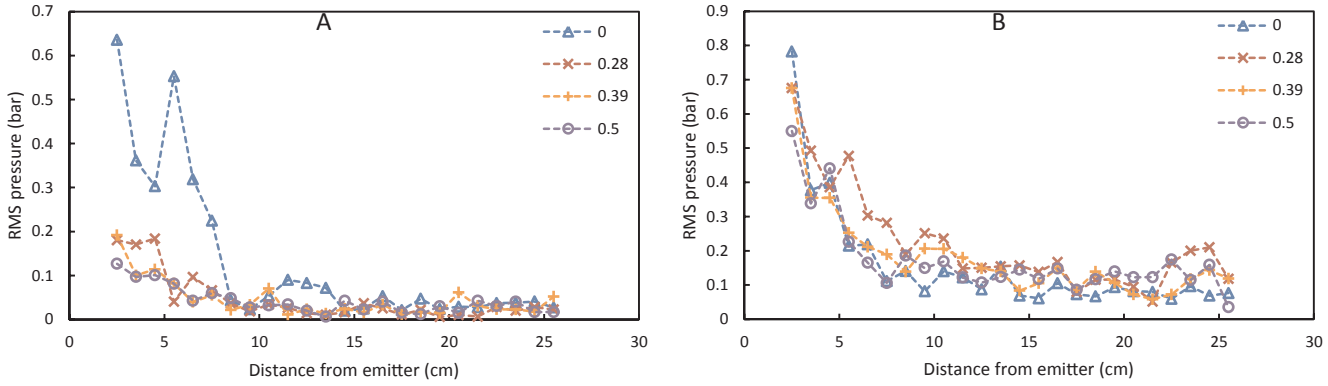

Fig. 14. Effect of the solid hold-up on the axial evolution of the RMS pressure calculated over different spectrum parts – case of glass particle suspension (2 mm diameter), emitted US power = 150 W – (A) Fundamental frequency – (B) Broad-band noise.

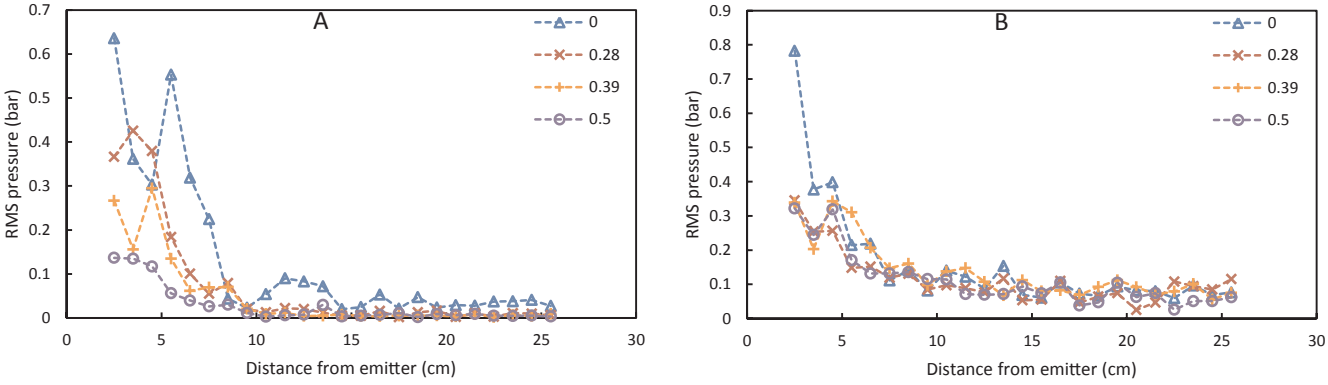

Fig. 15. Effect of the solid hold-up on the axial evolution of the RMS pressure calculated over different spectrum parts – case of plastic particle suspension (2 mm diameter), emitted US power = 150 W – (A) Fundamental frequency – (B) Broad-band noise.

spectrum power (Fig. 10B) increases in accordance with the emitted power. Such behavior is in fact due to an energy transfer from the fundamental toward the broad-band noise when increasing the emitted power, as shown in Fig. 10D. The contribution of the noise in the first 10*cm* indeed increases from less than 40% at 60 W to about 95% at 200 W (Fig. 11), suggesting a higher cavitation level. According to Yasui et al. [25], this comes with an increased numbers of bubbles, hindering also the propagation of the driving wave in the medium and leading to a faster decrease of the total power (acoustic shielding). On the other hand, the power of the (sub/ultra) harmonics (Fig. 10C) does not seem to be affected by the emitted power.

4.4. Effect of the liquid velocity

Over the explored range ($3.8\ cm.\ s^{-1} - 9.1\ cm.\ s^{-1}$), the liquid velocity does not have any significant effect on the measured profiles. However, there is a clear difference between the cases with and without flow. The curves of Fig. 12B show a higher value of the RMS pressure measured at the driving frequency when the liquid is flowing. A probable explanation is that the bubbles are swept away by the upward flow, hence reducing the acoustic shielding. This explanation seems confirmed by Fig. 12C, which shows less broad-band noise in this case, indicating less bubble activity. This thus lowers the contribution of the broad-band noise in the first 10 *cm*, from 85% in the quiescent liquid sonicated at 150 W to less than 60% when an upward flow is applied (see Fig. 13).

4.5. Effect of the particles

As the particles are much smaller than the wavelength (2 *mm* vs 7.5 *cm*), their effect on the wave attenuation should be mainly due to viscous losses, resulting from the oscillations of the particles in the surrounding medium, or to thermal dissipation loss, due to thermal gradients generated near the particle surface as the fluid undergoes non-isentropic periodic expansion-compression producing an oscillatory heat flow from/toward the particle [43,44]. Conversely, the effect of wave scattering should be negligible [45]. Considering their much higher relative density, larger attenuation would be expected for the glass beads compared to the polyamide ones in accordance with the measurements of Dukhin et al. on similar materials [46]. Table 2 gathers the attenuation coefficients corresponding to thermal losses (α_{th}) and viscous losses (α_{visc}). They have been estimated from the theoretical expressions available in Dukhin et al. [47] and He and Ni [48], respectively, and result in rather low values.

On the other hand, the particles could provide supplementary nuclei for cavitation or interact with the generated bubbles (according to their more or less hydrophobic surface state), leading to more complex trends. Fig. 14 shows the effect of glass particles on power attenuation (for the fundamental and broad-band noise, respectively), while Fig. 15 treats the case of polyamide beads. On these figures are recalled the profiles obtained without any solid at a liquid velocity of 6.1 cm/s (value required to achieve 40% of solid hold-up in the case of glass particles). It should be recalled that the surface of the expanded bed lies 1.5 *cm* away from the US emitter, and thus the solid particles should directly affect US propagation only beyond this distance. A strong additional wave damping is observed for the fundamental in the presence of particles, especially with glass beads. In the investigated range of solid hold-up (28–50%), its effect seems however lower for glass beads than plastic ones. This might be explained by the nonlinear dependence of the wave attenuation with respect to the solid hold-up above 10% vol., as observed by previous authors in the case of particles with high density contrast [46]. The effect on the broad-band noise (Figs. 14B and

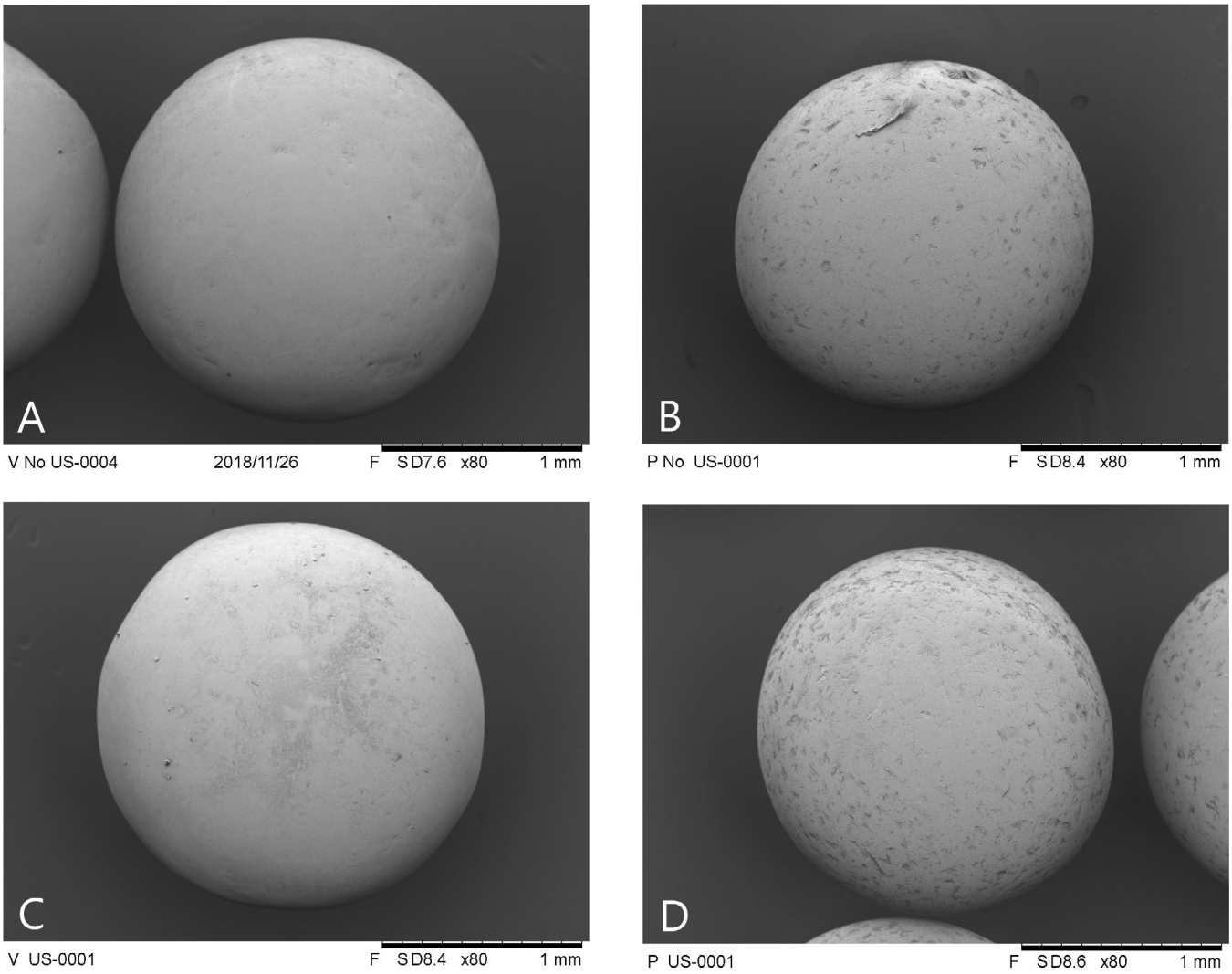

Fig. 16. MEB pictures of 2 mm glass and plastic particles before and after exposure to ultrasound – (A) Glass before US – (B) Plastic before US – (C) Glass after US – (D) Plastic after US.

15B) is rather different whether glass or plastic particles are considered. In the case of the glass particles, the corresponding profile is almost unchanged with or without solid, while the fundamental amplitude is fast below the abovementioned 20 kPa. This could indicate a lower cavitation threshold due to the nucleation sites brought by the particles, as concluded by Tuziuti et al. [49]. In the case of plastic particles, the noise is however significantly lower, despite their higher hydrophobicity and rugosity (see MEB pictures in Fig. 16) would be expected to enhance heterogeneous nucleation of bubbles. On the other hand, Crum and Brosey [50] observed that the cavitation threshold was increased by small amounts of polymer additive and explained this effect by a reduced surface tension using a Harvey-type model of cavitation nucleation. As seen on Fig. 16 plastic particles seem slightly eroded by US, suggesting that partial dissolution of polyamide might have occurred under US leading to a similar mechanism. The results with solid particles would require further exploration to be fully elucidated, and in particular to decorrelate their direct influence on wave attenuation from their indirect one via cavitation threshold (due to surface defects or partial dissolution). The fact remains that acoustic cavitation is in itself an open problem and that the diversity of possible interactions between particles and bubbles precludes a purely additive effect on attenuation.

5. Conclusions

A methodology has been developed for the acoustical characterization of sonoreactors, based on FFT signal processing, allowing to distinguish the different spectral components: driving frequency, (sub-/ultra-)harmonics corresponding to the stable cavitation and broad-band noise associated to the inertial one. The effect of increasing emitting power on the ultrasound propagation has been studied and the results indicate a higher energy transfer from the fundamental wave toward the broad-band noise, as well as a shielding effect by the cavitation bubbles leading to a fast decrease of the total signal power with the distance from the emitter. Hence it shows that the emission power in any sonochemistry process has to be carefully chosen as higher power does not necessarily imply higher efficiency. A probable explanation of the liquid flow effect is the sweeping of the cavitation bubbles away from the zone in front of the horn. Technical restrictions indeed implied to design this reactor with ultrasound emitted against the flow, but it could be interesting to work in other configurations to check if this trend would be then modified. The solid suspension brings additional attenuation, but it is much more difficult to conclude about the causes of the observed effects. In the light of the obtained results, this study could benefit from the use of an emitting device able to generate ultrasound at an intensity low enough to keep the medium below cavitation level (so as to uncouple for instance the respective effects of the

bubble cloud and of the solid particles on the wave attenuation).

This work will be followed by an experimental investigation of the local mass transfer coefficient (measured by electrochemical method) under the same conditions and in the same sonoreactor, so as to correlate its enhancement to the cavitation intensity and power repartition in the acoustic spectrum.

Acknowledgements

The authors thank B. Boyer and E. Prevot (LGC Toulouse) for technical support on the experimental setup and M.L. de Solan Bethmale (SAP, LGC Toulouse) for the MEB pictures of the particles.

References

[1] T.J. Mason, J.P. Lorimer, Applied Sonochemistry – The Uses of Power Ultrasound in Chemistry and Processing, Wiley-VCH, Weinheim, Germany, 2002.
[2] K.S. Suslick, Sonochemistry, Science 247 (1990) 1439–1445, https://doi.org/10.1126/science.247.4949.1439.
[3] S. Findik, G. Gündüz, E. Gündüz, Direct sonication of acetic acid in aqueous solutions, Ultrason. Sonochem. 13 (2006) 203–207, https://doi.org/10.1016/j.ultsonch.2005.11.005.
[4] M.M. van Iersel, N.E. Benes, J.T.F. Keurentjes, Importance of acoustic shielding in sonochemistry, Ultrason. Sonochem. 15 (2008) 294–300, https://doi.org/10.1016/j.ultsonch.2007.09.015.
[5] M. Sivakumar, A. Gedanken, Insights into the sonochemical decomposition of Fe(CO)5: theoretical and experimental understanding of the role of molar concentration and power density on the reaction yield, Ultrason. Sonochem. 11 (2004) 373–378, https://doi.org/10.1016/j.ultsonch.2003.08.002.
[6] V.S. Sutkar, P.R. Gogate, Design aspects of sonochemical reactors: Techniques for understanding cavitational activity distribution and effect of operating parameters, Chem. Eng. J. 155 (2009) 26–36, https://doi.org/10.1016/j.cej.2009.07.021.
[7] R.A. Al-Juboori, T. Yusaf, L. Bowtell, V. Aravinthan, Energy characterisation of ultrasonic systems for industrial processes, Ultrasonics 57 (2015) 18–30, https://doi.org/10.1016/j.ultras.2014.10.003.
[8] M. Hodnett, 8 - Measurement techniques in power ultrasonics, Power Ultrasonics, Woodhead Publishing, Oxford, 2015, pp. 195–218 (accessed April 19, 2016).
[9] R.F. Contamine, A.M. Wilhelm, J. Berlan, H. Delmas, Power measurement in sonochemistry, Ultrason. Sonochem. 2 (1995) S43–S47, https://doi.org/10.1016/1350-4177(94)00010-P.
[10] T.J. Mason, J.P. Lorimer, D.M. Bates, Quantifying sonochemistry: casting some light on a 'black art', Ultrasonics 30 (1992) 40–42, https://doi.org/10.1016/0041-624X(92)90030-P.
[11] S. Koda, T. Kimura, T. Kondo, H. Mitome, A standard method to calibrate sonochemical efficiency of an individual reaction system, Ultrason. Sonochem. 10 (2003) 149–156, https://doi.org/10.1016/S1350-4177(03)00084-1.
[12] A. Mandroyan, R. Viennet, Y. Bailly, M.-L. Doche, J.-Y. Hihn, Modification of the ultrasound induced activity by the presence of an electrode in a sonoreactor working at two low frequencies (20 and 40kHz). Part I: active zone visualization by laser tomography, Ultrason. Sonochem. 16 (2009) 88–96, https://doi.org/10.1016/j.ultsonch.2008.05.003.
[13] G. Mark, A. Tauber, R. Laupert, H.-P. Schuchmann, D. Schulz, A. Mues, C. von Sonntag, OH-radical formation by ultrasound in aqueous solution – Part II: terephthalate and Fricke dosimetry and the influence of various conditions on the sonolytic yield, Ultrason. Sonochem. 5 (1998) 41–52, https://doi.org/10.1016/S1350-4177(98)00012-1.
[14] B. Zeqiri, M. Hodnett, A.J. Carroll, Studies of a novel sensor for assessing the spatial distribution of cavitation activity within ultrasonic cleaning vessels, Ultrasonics 44 (2006) 73–82, https://doi.org/10.1016/j.ultras.2005.08.004.
[15] A.E. Crawford, The measurement of cavitation, Ultrasonics 2 (1964) 120–123, https://doi.org/10.1016/0041-624X(64)90224-0.
[16] K. Yasui, T. Tuziuti, M. Sivakumar, Y. Iida, Sonoluminescence, Appl. Spectrosc. Rev. 39 (2004) 399–436, https://doi.org/10.1081/ASR-200030202.
[17] C.J.B. Vian, P.R. Birkin, T.G. Leighton, Cluster collapse in a cylindrical cell: correlating multibubble sonoluminescence, acoustic pressure, and erosion, J. Phys. Chem. C 114 (2010) 16416–16425, https://doi.org/10.1021/jp1027977.
[18] M. Ashokkumar, The characterization of acoustic cavitation bubbles – an overview, Ultrason. Sonochem. 18 (2011) 864–872, https://doi.org/10.1016/j.ultsonch.2010.11.016.
[19] D. Fernandez Rivas, M. Ashokkumar, T. Leong, K. Yasui, T. Tuziuti, S. Kentish, D. Lohse, H.J.G.E. Gardeniers, Sonoluminescence and sonochemiluminescence from a microreactor, Ultrason. Sonochem. 19 (2012) 1252–1259, https://doi.org/10.1016/j.ultsonch.2012.04.008.
[20] E. Cramer, W. Lauterborn, Acoustic cavitation noise spectra, Appl. Sci. Res. 38 (1982) 209–214, https://doi.org/10.1007/BF00385950.
[21] C. Campos-Pozuelo, C. Granger, C. Vanhille, A. Moussatov, B. Dubus, Experimental and theoretical investigation of the mean acoustic pressure in the cavitation field, Ultrason. Sonochem. 12 (2005) 79–84, https://doi.org/10.1016/j.ultsonch.2004.06.009.
[22] V.S. Moholkar, S.P. Sable, A.B. Pandit, Mapping the cavitation intensity in an ultrasonic bath using the acoustic emission, AIChE J. 46 (2000) 684–694, https://doi.org/10.1002/aic.690460404.
[23] J. Frohly, S. Labouret, C. Bruneel, I. Looten-Baquet, R. Torguet, Ultrasonic cavitation monitoring by acoustic noise power measurement, J. Acoust. Soc. Am. 108 (2000) 2012–2020, https://doi.org/10.1121/1.1312360.
[24] Z. Liang, G. Zhou, S. Lin, Y. Zhang, H. Yang, Study of low-frequency ultrasonic cavitation fields based on spectral analysis technique, Ultrasonics 44 (2006) 115–120, https://doi.org/10.1016/j.ultras.2005.09.001.
[25] K. Yasui, T. Tuziuti, J. Lee, T. Kozuka, A. Towata, Y. Iida, Numerical simulations of acoustic cavitation noise with the temporal fluctuation in the number of bubbles, Ultrason. Sonochem. 17 (2010) 460–472, https://doi.org/10.1016/j.ultsonch.2009.08.014.
[26] M. Hodnett, R. Chow, B. Zeqiri, High-frequency acoustic emissions generated by a 20 kHz sonochemical horn processor detected using a novel broadband acoustic sensor: a preliminary study, Ultrason. Sonochem. 11 (2004) 441–454, https://doi.org/10.1016/j.ultsonch.2003.09.002.
[27] M. Hodnett, B. Zeqiri, Toward a reference ultrasonic cavitation vessel: Part 2-investigating the spatial variation and acoustic pressure threshold of inertial cavitation in a 25 kHz ultrasound field, IEEE Trans. Ultrason. Ferroelectr. Freq. Control 55 (2008) 1809–1822, https://doi.org/10.1109/TUFFC.2008.864.
[28] T. Uchida, H. Sato, S. Takeuchi, T. Kikuchi, Investigation of output signal from cavitation sensor by dissolved oxygen level and sonochemical luminescence, Jpn. J. Appl. Phys. 49 (2010) 07HE03, https://doi.org/10.1143/JJAP.49.07HE03.
[29] T. Uchida, S. Takeuchi, T. Kikuchi, Measurement of amount of generated acoustic cavitation: investigation of spatial distribution of acoustic cavitation generation using broadband integrated voltage, Jpn. J. Appl. Phys. 50 (2011) 07HE01, https://doi.org/10.1143/JJAP.50.07HE01.
[30] T. Thanh Nguyen, Y. Asakura, S. Koda, K. Yasuda, Dependence of cavitation, chemical effect, and mechanical effect thresholds on ultrasonic frequency, Ultrason. Sonochem. 39 (2017) 301–306, https://doi.org/10.1016/j.ultsonch.2017.04.037.
[31] J.R. Allegra, S.A. Hawley, Attenuation of sound in suspensions and emulsions: theory and experiments, J. Acoust. Soc. Am. 51 (1972) 1545–1564, https://doi.org/10.1121/1.1912999.
[32] C.M. Atkinson, H.K. Kytömaa, Acoustic wave speed and attenuation in suspensions, Int. J. Multiphase Flow 18 (1992) 577–592, https://doi.org/10.1016/0301-9322(92)90053-J.
[33] L. Gaete-Garretón, Y. Vargas-Hernández, S. Pino-Dubreuil, F. Montoya-Vitini, Ultrasonic detectors for high-intensity acoustic fields, Sens. Actuators, A 37–38 (1993) 410–414, https://doi.org/10.1016/0924-4247(93)80070-W.
[34] M. Cerna, A.F. Harvey, The Fundamentals of FFT-based Signal Analysis and Measurement, National Instruments Application Note 041, 2000.
[35] J.P. Riba, R. Routie, J.P. Couderc, Conditions minimales de mise en fluidisation par un liquide, Can. J. Chem. Eng. 56 (1978) 26–30, https://doi.org/10.1002/cjce.5450560104.
[36] R. Di Felice, Hydrodynamics of liquid fluidisation, Chem. Eng. Sci. 50 (1995) 1213–1245, https://doi.org/10.1016/0009-2509(95)98838-6.
[37] S. Ergun, Fluid flow through packed columns, Chem. Eng. Prog. 48 (1952) 89–94.
[38] C.Y. Wen, Y.H. Yu, Mechanics of Fluidization, Chem. Eng. Prog. Symp. Ser. 62 (1966) 100–111.
[39] Y. Son, M. Lim, J. Khim, M. Ashokkumar, Acoustic emission spectra and sonochemical activity in a 36kHz sonoreactor, Ultrason. Sonochem. 19 (2012) 16–21, https://doi.org/10.1016/j.ultsonch.2011.06.001.
[40] F. Burdin, N.A. Tsochatzidis, P. Guiraud, A.M. Wilhelm, H. Delmas, Characterisation of the acoustic cavitation cloud by two laser techniques, Ultrason. Sonochem. 6 (1999) 43–51, https://doi.org/10.1016/S1350-4177(98)00035-2.
[41] R. Mettin, S. Luther, W. Lauterborn, Bubble size distribution and structures in acoustic cavitation, in: Proceedings of 2nd Conference on Applications of Power Ultrasound in Physical and Chemical Processing, Toulouse, France, 1999, pp. 125–129.
[42] O. Louisnard, A simple model of ultrasound propagation in a cavitating liquid. Part I: theory, nonlinear attenuation and traveling wave generation, Ultrason. Sonochem. 19 (2012) 56–65, https://doi.org/10.1016/j.ultsonch.2011.06.007.
[43] P.S. Epstein, R.R. Carhart, The absorption of sound in suspensions and emulsions. I. Water fog in air, J. Acoust. Soc. Am. 25 (1953) 553–565, https://doi.org/10.1121/1.1907107.
[44] P.M. Morse, K.U. Ingard, Theoretical Acoustics, Princeton University Press, 1986.
[45] M. Su, M. Xue, X. Cai, Z. Shang, F. Xu, Particle size characterization by ultrasonic attenuation spectra, Particuology 6 (2008) 276–281, https://doi.org/10.1016/j.partic.2008.02.001.
[46] A.S. Dukhin, P.J. Goetz, Acoustic spectroscopy for concentrated polydisperse colloids with high density contrast, Langmuir 12 (1996) 4987–4997, https://doi.org/10.1021/la951085y.
[47] A.S. Dukhin, P.J. Goetz, C.W. Hamlet, Acoustic spectroscopy for concentrated polydisperse colloids with low density contrast, Langmuir 12 (1996) 4998–5003, https://doi.org/10.1021/la951572d.
[48] G. He, W. Ni, Ultrasonic attenuation model for measuring particle size and inverse calculation of particle size distribution in mineral slurries, J Cent. South Univ. Technol. 13 (2006) 445–450, https://doi.org/10.1007/s11771-006-0065-x.
[49] T. Tuziuti, K. Yasui, M. Sivakumar, Y. Iida, N. Miyoshi, Correlation between acoustic cavitation noise and yield enhancement of sonochemical reaction by particle addition, J. Phys. Chem. A 109 (2005) 4869–4872, https://doi.org/10.1021/jp0503516.
[50] L.A. Crum, J.E. Brosey, Effect of dilute polymer additives on the acoustic cavitation threshold of water, J. Fluids Eng. 106 (1984) 99–104, https://doi.org/10.1115/1.3242413.